

# Revealing Nanomechanical Domains and Their Transient Behavior in Mixed-Halide Perovskite Films

Ioanna Mela, Chetan Poudel, Miguel Anaya,\* Géraud Delport, Kyle Frohna, Stuart Macpherson, Tiarnan A. S. Doherty, Anna Scheeder, Samuel D. Stranks,\* and Clemens F. Kaminski\*


Halide perovskites are a versatile class of semiconductors employed for high performance emerging optoelectronic devices, including flexoelectric systems, yet the influence of their ionic nature on their mechanical behavior is still to be understood. Here, a combination of atomic-force, optical, and compositional X-ray microscopy techniques is employed to shed light on the mechanical properties of halide perovskite films at the nanoscale. Mechanical domains within and between morphological grains, enclosed by mechanical boundaries of higher Young's Modulus (YM) than the bulk parent material, are revealed. These mechanical boundaries are associated with the presence of bromide-rich clusters as visualized by nano-X-ray fluorescence mapping. Stiffer regions are specifically selectively modified upon light soaking the sample, resulting in an overall homogenization of the mechanical properties toward the bulk YM. This behavior is attributed to light-induced ion migration processes that homogenize the local chemical distribution, which is accompanied by photobrightening of the photoluminescence within the same region. This work highlights critical links between mechanical, chemical, and optoelectronic characteristics in this family of perovskites, and demonstrates the potential of combinational imaging studies to understand and design halide perovskite films for emerging applications such as photoflexoelectricity.

## 1. Introduction

Since 2009, halide perovskites have emerged as promising materials for efficient optoelectronic devices such as photovoltaics

Dr. I. Mela, Dr. C. Poudel, Dr. M. Anaya, Dr. S. D. Stranks,  
Prof. C. F. Kaminski  
Department of Chemical Engineering & Biotechnology  
University of Cambridge  
Philippa Fawcett Drive, Cambridge CB3 0AS, UK  
E-mail: sds65@cam.ac.uk; cfk23@cam.ac.uk

Dr. M. Anaya, Dr. G. Delport, K. Frohna, S. Macpherson, T. A. S. Doherty,  
A. Scheeder, Dr. S. D. Stranks  
Cavendish Laboratory  
University of Cambridge  
JJ Thomson Avenue, Cambridge CB3 0HE, UK  
E-mail: ma811@cam.ac.uk

 The ORCID identification number(s) for the author(s) of this article can be found under <https://doi.org/10.1002/adfm.202100293>.

© 2021 The Authors. Advanced Functional Materials published by Wiley-VCH GmbH. This is an open access article under the terms of the Creative Commons Attribution License, which permits use, distribution and reproduction in any medium, provided the original work is properly cited.

DOI: 10.1002/adfm.202100293

and light-emitting diodes (LEDs),<sup>[1–3]</sup> with performance in some configurations already exceeding comparable existing commercial technologies.<sup>[4,5]</sup> Halide perovskite semiconductors show unique properties such as remarkable defect tolerance,<sup>[6]</sup> efficient light absorption<sup>[7,8]</sup> and long charge-carrier diffusion lengths,<sup>[9–11]</sup> which put them at the forefront of emerging thin-film technologies. One advantage they have over conventional semiconductors is that they can be fabricated through facile and cost-effective preparation techniques (e.g., solution processing), with the precursor components self-assembling into relatively large entities (domains of ≈0.1 to several micrometers in size,<sup>[12]</sup> referred to as grains). Moreover, the organic–inorganic hybrid nature of these materials enables a wide variety of possibilities in terms of compositional management<sup>[13,14]</sup> to tailor their properties to a given application. Variability associated with current preparation techniques combined with this compositional tuning give rise to complex heterogeneity across multiple length scales,<sup>[15–17]</sup> including variations in morphological, structural, and photophysical properties.

In particular, state-of-the-art halide perovskite devices are based on multication (methylammonium, MA; formamidinium, FA; cesium, Cs) mixed-halide (Bromide, Br; Iodide, I) compositions,<sup>[18]</sup> such as the “triple cation” composition  $\text{Cs}_{0.05}\text{MA}_{0.17}\text{FA}_{0.78}\text{Pb}(\text{I}_{0.83}\text{Br}_{0.17})_3$ . These compositions are relevant not only for single junction devices but also for tandem solar cells in which the perovskite top cells are inevitably mixed halide, mixed cation perovskite compositions to achieve suitably wide bandgaps.<sup>[19]</sup> The alloyed nature of these films tends to generate local variations of the chemical composition at the nanoscale, as observed by electron and X-ray microscopy techniques.<sup>[20–22]</sup> These compositional heterogeneities correlate directly with crystallographically distinct entities, generating nanoscopic interfaces where discrete deep trap clusters are prominent.<sup>[16]</sup> Control over the resulting compositional variations represents a promising strategy to tailor transport of excited species<sup>[3]</sup> or photodoping<sup>[23]</sup> and make use of the full potential of these alloyed halide perovskites. Photoinduced chemical reorganization of the halides adds another layer of complexity that can either be problematic for operation,<sup>[24]</sup> or desirable, for example to form composition gradients or to

passivate defects.<sup>[25,26]</sup> Additionally, recent reports suggest that strain gradients in these materials play a crucial role in the final performance of devices,<sup>[27,28]</sup> which, in turn, may show a strong flexoelectric response substantially boosted by photoexcitation.<sup>[29]</sup> For these reasons, understanding the mechanical properties of these semiconductors and their link to compositional variations, light exposure, and thus photophysical performance is generating widespread interest in the research community.

Halide perovskites are substantially softer materials<sup>[30,31]</sup> (Young's Modulus (YM) below 20 GPa) than purely inorganic semiconductors such as Si, GaAs,<sup>[32]</sup> CIGS,<sup>[33]</sup> or other oxide perovskites<sup>[33]</sup> (YM on the order of hundreds of GPa). This softness suggests that applying small mechanical stresses might lead to a significant motion of ions in the crystal, and vice versa, through, for instance, photoinduced chemical changes. Indeed, indentation measurements have demonstrated that the YM of single halide perovskites strongly depends on the strength of the Pb–halide bond.<sup>[33–35]</sup> This observation may translate into nanoscale variations of the mechanical properties in more complex mixed-halide perovskites, depending on their local halide distribution.<sup>[26]</sup> However, access to nanoscopic mechanical information is elusive for traditional indentation methods, and thus there remains a limited understanding of local mechanical properties in state-of-the-art mixed-halide perovskites and their behavior under light exposure. Such an understanding is, however, critical for further device improvements and for the realization of new device paradigms, including straintronics<sup>[36,37]</sup> or flexoelectric devices.<sup>[38]</sup>

Here, we use quantitative nanomechanical mapping (QNM) atomic force microscopy (AFM) to simultaneously map the morphology and quantify the local YM of triple-cation, mixed-halide Cs<sub>0.05</sub>MA<sub>0.17</sub>FA<sub>0.78</sub>Pb(I<sub>0.83</sub>Br<sub>0.17</sub>)<sub>3</sub> perovskite films. These measurements reveal unexpected variations in the YM, as large as one order of magnitude over just a few tens of nanometers. We observe distinct high YM inter- and intra-grain features, which are identified as bromide-rich regions by nano X-ray fluorescence (nXRF) chemical mapping, and define mechanical domains. Correlative time-resolved photoluminescence imaging measurements (see Experimental Section for technical details of the experiment) shows an overall increase of the charge carrier lifetime upon light soaking, which is accompanied by a decrease of the YM of the stiffer entities toward the bulk YM values. This observation suggests that the ionic character confers these materials with transient mechanical behavior at the nanoscale under operando conditions, impacting their photophysical performance. Control over these properties will be critical to stabilizing halide perovskites for their integration in emerging optoelectronic devices, especially those involving both light and mechanical phenomena.<sup>[39]</sup>

## 2. Results and Discussion

Cs<sub>0.05</sub>MA<sub>0.17</sub>FA<sub>0.78</sub>Pb(I<sub>0.83</sub>Br<sub>0.17</sub>)<sub>3</sub> perovskite thin films were fabricated on glass coverslips following standard solution processing methods (see Experimental Section for details and Figures S1–S3, Supporting Information, for morphological, structural, and steady-state photoluminescence, PL, characterization). We employ a modular setup to extract mechanical

(QNM-AFM mode) and photophysical (time-resolved PL mode) properties of the same region of interest in our films. A sequential methodology between these modes is followed to always map the same perovskite–air interface and ensure appropriate comparisons (see Experimental Section and Figure S4, Supporting Information, for an explanation on the methodology). QNM-AFM allows to simultaneously acquire high-resolution (10 × 10 nm<sup>2</sup>) topography (Figure 1a) and YM (Figure 1b) maps of the perovskite thin film (see Experimental Section and Figure S5, Supporting Information). An advantage of this approach compared to traditional indentation is that QNM-AFM does not plastically deform the sample, and therefore does not induce changes in the perovskite material during measurements<sup>[40–42]</sup> (Figure S6, Supporting Information). In addition, we use the time-resolved PL mode of our setup to obtain diffraction-limited PL images across the same area of the sample, providing valuable information about the local dynamics of charge carriers in the perovskite films even though its spatial resolution is lower than that of AFM. A typical time-resolved PL image is shown in Figure S7, Supporting Information, and reveals a mean PL lifetime of 154.4 ± 43.7 ns, in agreement with previous observations for similar excitation fluences<sup>[43,44]</sup> and also an indication of the high quality of the fabricated films (see Experimental Section).

Using the topography images in Figure 1a, we identify large domains (associated with height local maxima) that are defined as morphological grains separated by grain boundaries (associated with height local minima). The lateral size of these morphological grains ranges between one and several hundreds of nanometers, which is similar in size to the morphological grains measured by scanning electron microscopy (Figure S1, Supporting Information). Interestingly, the nanomechanical map (Figure 1b) reveals substantial YM variations across the sample, ranging between 2 and 25 GPa, and provides the first demonstration of local variations in the stiffness of perovskite films. Moreover, our measurements not only show that interfaces between morphological grains are generally higher in YM (intergrain features) but also unveil smaller mechanical subdomains (intragrain features). This observation is further highlighted in Figure 1c, where topography and YM maps are overlaid, and in Figure 1d, where the variation in height and YM in the sample across a line profile (as defined by the blue dotted line in Figure 1a–c) is displayed. Mechanical domains are enclosed by regions of higher YM that are denominated as mechanical boundaries hereafter. This behavior is reproduced in multiple mixed halide samples (see Figure S8, Supporting Information) and in pure-iodide samples (see Figure S9, Supporting Information). The existence of intragrain mechanical domains can potentially be linked with the recent observation of structural features within morphological grains, which can impact optoelectronic performance of these materials.<sup>[21,45]</sup>

To quantify the variations in YM, we break the data obtained by QNM-AFM down to values acquired from bulk areas and those acquired from the mechanical boundaries, based on the YM maps. We find spatially averaged values of YM to be 9.1 ± 2.6 GPa but observe significant differences between the YM in bulk sites (6.9 ± 1.3 GPa) and the YM at the mechanical boundaries (12.5 ± 2.9 GPa) (Figure 1e). In order to identify the origin of such mechanical variations, we explore how

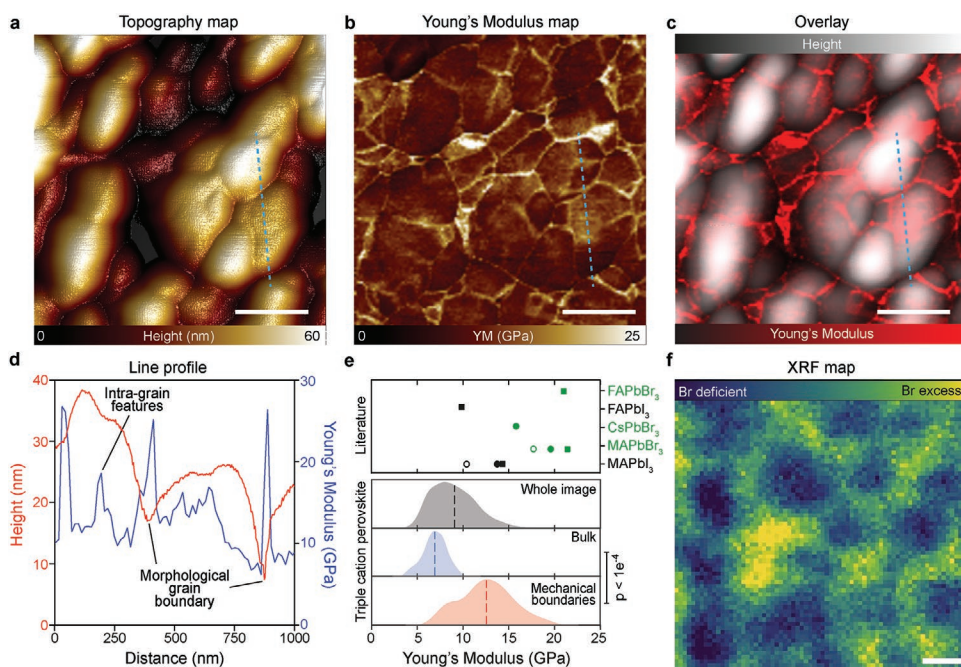


**Figure 1.** QNM-AFM mapping of  $\text{Cs}_{0.05}\text{MA}_{0.17}\text{FA}_{0.78}\text{Pb}(\text{I}_{0.83}\text{Br}_{0.17})_3$  perovskite thin films. a) Topography maps of the perovskite film show distinct morphological grains. b) YM map of the same sample area. c) Overlay of the Topography (a) and YM (b) maps, revealing the existence of subdomains of different stiffness within individual morphological grains. d) Line profile across two morphological grains (highlighted with blue dotted line in Figure 1a–c) shows the height profile (in red) and the Young's modulus profile (in blue). e) Macroscopic YM values reported in the literature<sup>[31,33,34]</sup> on halide perovskite single crystals of different compositions (each containing a single halide and a single monovalent cation). These values are comparable to the spatially averaged values obtained from our  $\text{Cs}_{0.05}\text{MA}_{0.17}\text{FA}_{0.78}\text{Pb}(\text{I}_{0.83}\text{Br}_{0.17})_3$  perovskite thin films. Histograms of the YM values across the whole image shown in panel (b) (in black) and separately for the regions identified as bulk (blue) or as mechanical boundaries (red) ( $p < 10^{-4}$ , unpaired two-tailed *t*-test). f) Compositional map showing normalized Br:Pb ratio extracted from nXRF peak intensities. We note that the areas shown in nXRF and AFM are not spatially correlated. The color scale is linear, with darker areas representing regions with lower amount of bromide. All scale bars correspond to 500 nm.

they are connected to compositional heterogeneities that arise during the thin-film fabrication.<sup>[25,46]</sup> Although there is limited literature on the mechanical properties of halide perovskites, it has been reported that the macroscopic YM of these materials strongly depend on the halide content (summarized in the top panel in Figure 1e).<sup>[31,33,34]</sup> Specifically, the pure bromide-based perovskites show significantly larger YM values than their I-based counterparts: 17.5–19.6 GPa for MAPbBr<sub>3</sub> compared to 10–14.3 GPa for MAPbI<sub>3</sub>.<sup>[33,47,48]</sup> This difference in YM has been proposed to be associated with the higher Br–Pb bond strength in comparison to that of the I–Pb bond.<sup>[35]</sup> Moreover, Hutter et al. have reported macroscopic YM values for the iodide–bromide mixtures that lie between those of the pure bromide and iodide samples.<sup>[47]</sup> Although these macroscopic YMs were obtained by invasive techniques such as indentation, they correlate well with the spatially averaged values measured across our mixed-halide films. We hypothesize that local halide content has a direct influence on the local YM of mixed-halide films.<sup>[47]</sup> Indeed, Figure 1e shows that the bulk YM values are very close to the reported values for the pure iodide-based perovskites, while the values at the mechanical boundaries tend to be comparable to those for pure bromide-based perovskites. This hypothesis is confirmed through our QNM-AFM measurements on pure-iodide samples (see Figure S9, Supporting Information), where we show that their overall YM is significantly lower than that of the mixed halide ones ( $3.45 \pm 0.42$  vs  $9.1 \pm 2.6$  GPa). In addition,

YM variations (boundaries to bulk) are much less pronounced in pure-iodide samples, as would be expected. This observation is highlighted in Figure S10, Supporting Information, where we directly compare samples of different halide content. YM values for pure-iodide samples correspond to the lowest end of the distribution of the YM in mixed-halide samples. This result indicates the dominant role of bromide on the YM of mixed halide films, even though there is only 15% of nominal bromide in the composition. To further validate this proposition we mapped the Br-to-Pb ratio in our mixed-halide perovskite films using nXRF microscopy. Fluorescence was excited using a nanoprobe synchrotron source and a spatial resolution of 50 nm was obtained. Figure 1f shows a distinct bromide content heterogeneity in the films, with bromide accumulation in specific sites that appear to be grain interfaces.<sup>[46]</sup> We do also see some grains (e.g., the yellow spot in Figure 1f) that appear bromide-rich, and likewise we also see some grain interiors that have changed mechanical properties (see Figure 1b). However, the majority of the mechanical properties are elevated in the boundaries and this tracks with the majority of bromide sitting in boundaries in the chemical map. We therefore conclude that many of the mechanical boundaries (either morphological grain boundaries or subgrain features) present higher bromide content while most of the remaining material is consistent with having an iodide-rich  $\text{Cs}_{0.05}\text{MA}_{0.17}\text{FA}_{0.78}\text{Pb}(\text{I}_{0.83}\text{Br}_{0.17})_3$  formulation, as shown in the YM maps.



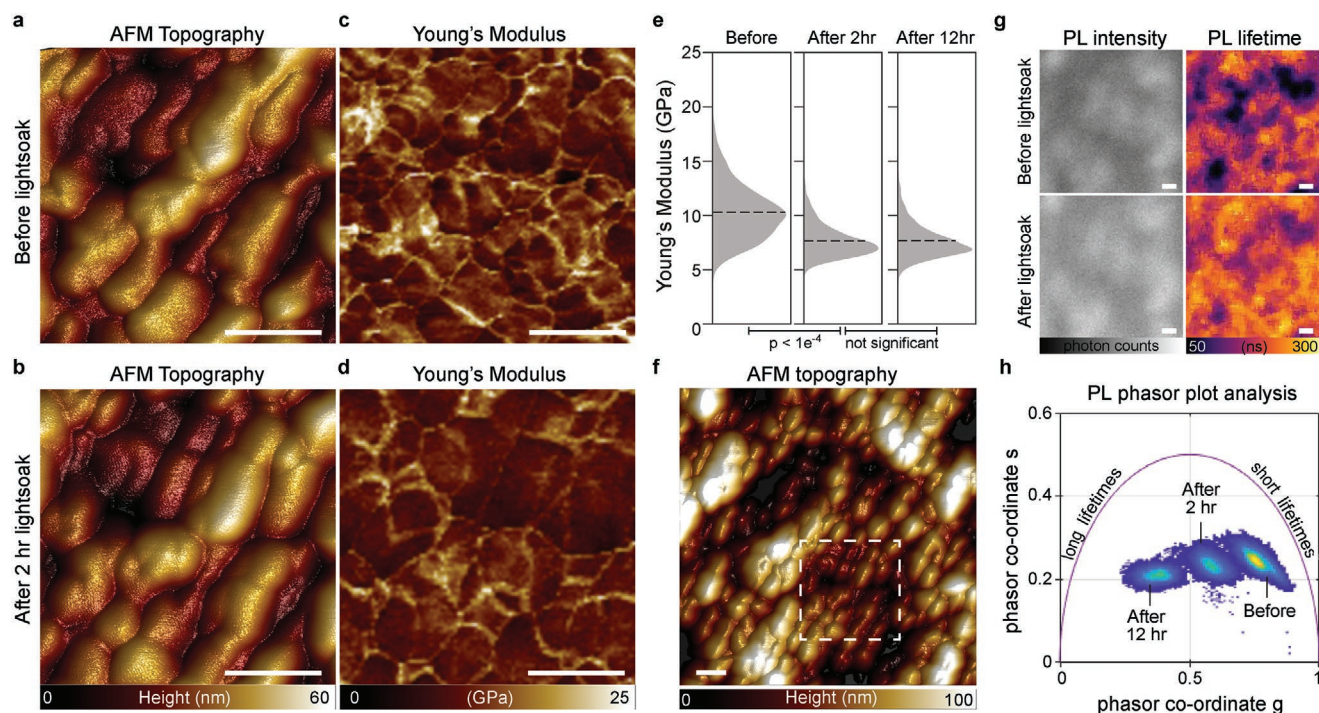


**Figure 2.** Atomic force microscopy and photoluminescence lifetime microscopy reveal changes in the mechanical properties and the emission lifetime of  $\text{Cs}_{0.05}\text{MA}_{0.17}\text{FA}_{0.78}\text{Pb}(\text{I}_{0.83}\text{Br}_{0.17})_3$  perovskite thin films. a,c) AFM topography and YM maps of the sample before light-soaking. b,d) AFM topography and YM maps of the same area after 2 h of white light soaking ( $\approx 375 \text{ mW cm}^{-2}$ ). While the topography of the sample remains largely unchanged, the YM values show significant homogenization. e) Histograms showing a significant lowering and homogenization of YM values upon 2 and 12 h of light soaking. f) AFM topography map of a  $5 \times 5 \mu\text{m}^2$  area of the perovskite film. Topography and YM maps of the  $2 \times 2 \mu\text{m}^2$  region marked by dotted lines were investigated in (a–d). g) Time-resolved PL maps of the same region as the AFM topography map in (f) shows photobrightening and an increase in PL lifetimes upon 2 h of light soaking. h) Phasor plot of time-resolved PL data showing a significant increase in PL lifetimes upon 2 h of light soaking and a further increase upon 12 h of light soaking for all areas in the illuminated region. All scale bars: 500 nm.

It is known that light soaking induces halide migration in perovskite thin films, an effect that has a large influence on the performance of perovskite-based optoelectronic devices.<sup>[26]</sup> Given the connection between the local mechanical properties and local halide content in mixed-halide perovskites revealed, these properties are expected to evolve when exposing the films to light. We perform correlative QNM-AFM and FLIM measurements on  $\text{Cs}_{0.05}\text{MA}_{0.17}\text{FA}_{0.78}\text{Pb}(\text{I}_{0.83}\text{Br}_{0.17})_3$  films after light soaking them for 2 and 12 h under continuous white-light illumination with an intensity of  $\approx 375 \text{ mW cm}^{-2}$  (Figure 2). This mild illumination condition,  $\approx 3.75$  times the intensity of natural sunlight on the Earth's surface, allows us to evaluate the impact of light on the mechanical and photo-physical properties of the films without damaging the material. QNM-AFM maps acquired before (Figure 2a) and after (Figure 2b) illumination show that the topography of the film exhibits small changes in height after 2 h of continuous illumination in laboratory ambient conditions. However, the corresponding YM maps reveal much larger modifications in the local mechanical properties of the sample (Figure 2c,d), with an overall reduction in the number of mechanical boundaries. This effect leads to a merging of adjacent mechanical domains and an increase in their effective size, resulting in a mechanical homogenization over the film after light soaking. Figure 2e displays a significant decrease in the spatially averaged YM from  $10.3 \pm 2.7$  to  $7.6 \pm 1.4$  GPa after 2 h of light soaking, with no

further significant changes noticeable after 12 h of illumination ( $7.6 \pm 1.5$  GPa). The spatially averaged YM after light soaking is very close to the average calculated for the bulk ( $6.9 \pm 1.3$  GPa) in Figure 1e, indicating further that there is homogenization of the YM of the sample toward the lower values.

To provide another perspective on the evolution of the physical properties of the film, we performed correlative time-resolved PL imaging and AFM on the same scan region (Figures 2f and 2g, respectively). These figures show a larger area ( $5 \times 5 \mu\text{m}^2$ ) encompassing the ( $2 \times 2 \mu\text{m}^2$ ) areas in Figure 2a–d, where the QNM analysis was performed. Upon light soaking, these FLIM maps of the perovskite film show an increase in both luminescence intensity (photobrightening) and PL lifetime (Figure 2g and Figure S11, Supporting Information, for PL decay curves). The changes in PL lifetime originate from the extended white-light soaking and not from the pulsed laser illumination used to acquire the PL maps (Figure S12, Supporting Information). Changes in PL lifetime are also visualized using phasor plots,<sup>[49,50]</sup> which provide a global graphical representation of time-resolved data in every pixel without needing to invoke any physical models (see Experimental Section for a description of how phasor coordinates are calculated from time-resolved data). Importantly, the phasor plot reveals a trajectory of all pixels toward longer PL lifetimes (successive movement to the left) upon 2 and 12 h of sample illumination. This enhancement in the PL of the films in ambient

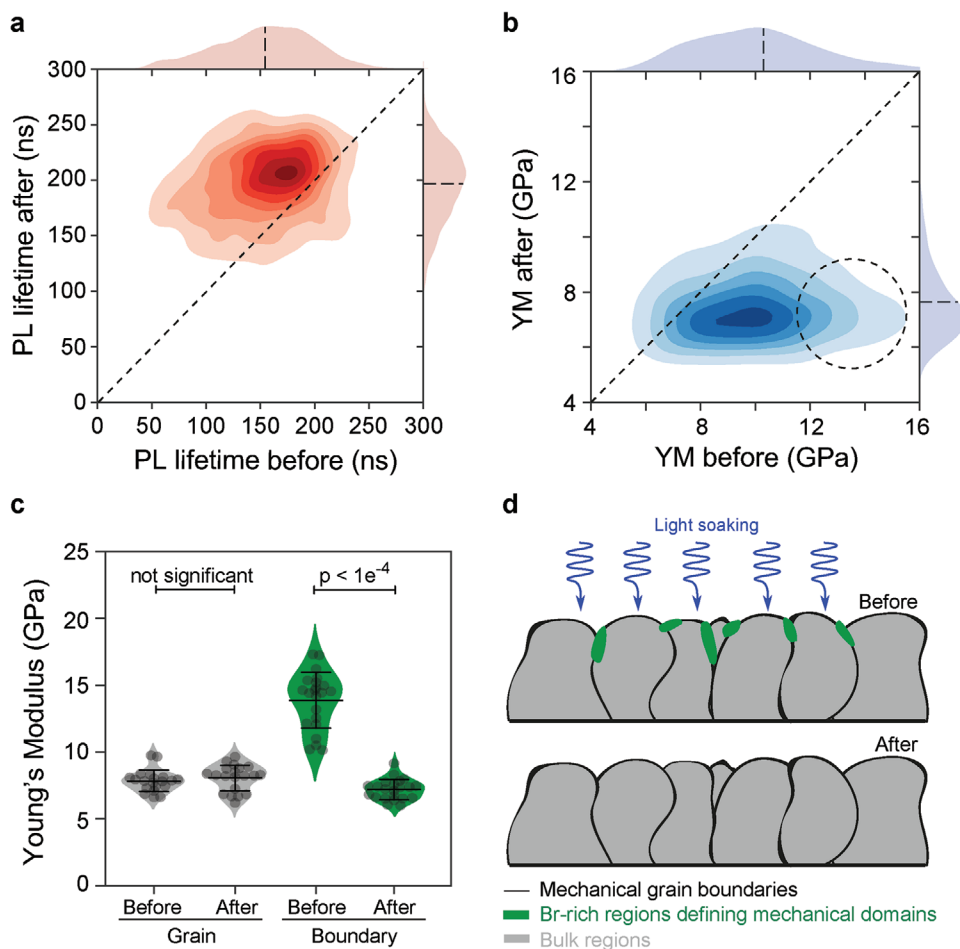


**Figure 3.** Material and photophysical properties of  $\text{Cs}_{0.05}\text{MA}_{0.17}\text{FA}_{0.78}\text{Pb}(\text{I}_{0.83}\text{Br}_{0.17})_3$  perovskite thin films before and after light soaking. a) Pixel-by-pixel comparison and histograms of the PL lifetimes show a significant overall increase in the PL lifetimes after 2 h of light soaking with white light at  $\approx 375 \text{ mW cm}^{-2}$ . b) Pixel-by-pixel comparison and histograms of the YM show an overall reduction, especially of the higher stiffness values (dashed circle), after 2 h of light soaking. c) Distinct softening of the mechanical boundaries is observed after 2 h of light soaking. The stiffness of the bulk regions of the morphological grain does not change. d) Schematic representation of the cross section of a triple cation mixed-halide perovskite film exhibiting several grains. Light-soaking induces a motion of the halides, leading to a homogenization of the halide (iodide/bromide) ratio. In particular, it smooths out the large bromide-rich clusters into the bulk, thus inducing a decrease of the YM values measured at the mechanical boundaries.

atmosphere is in good agreement with the literature<sup>[26]</sup> under these illumination conditions, which is linked to photo-chemical reactions involving oxygen species, moisture, and mobile halides/defects that passivate trap states. Here, these observations correlate well with a homogenization of the mechanical properties of the material.

A pixel-by-pixel comparison and histograms of the PL lifetimes before and after illumination (Figure 3a) reveal a significant overall increase in the PL lifetime from  $154 \pm 44$  to  $197 \pm 33$  ns after light soaking ( $p < 1e^{-4}$ , paired two-tailed *t*-test). The same analysis for YM values (Figure 3b) shows that there is a light-induced reduction in the YM of the sample, with the most pronounced reduction in the regions that are initially of high stiffness (highlighted by a dashed circle). We then separately quantify the YM associated with bulk areas before and after 2 h of light exposure (Figure 3c). This analysis shows that the bulk areas that initially present low YM remain largely unchanged in terms of stiffness ( $7.8 \pm 0.8$  and  $8.0 \pm 0.8$  GPa before and after light soaking, respectively). However, the mechanical boundaries

undergo a significant reduction in YM ( $13.8 \pm 2.1$  GPa before and  $7.1 \pm 0.8$  GPa after light soaking), which can also be extracted from Figure 3b (see dashed circle). The YM of the mechanical boundaries tends to converge toward the spatially averaged YM of the bulk sites, effectively leading to a homogenization of the YM across the thin film. These results are seen in multiple batches, with statistical results from all samples ( $n = 3$  batches, 3 samples scanned in each) included in Figure 3c.

Taking the collective findings into account, we propose that our as-formed material contains halide-rich regions,<sup>[51]</sup> which are much more pronounced in mixed-halide perovskites. For example, bromide accumulation resides preferentially at the boundaries of morphological grains but also occurs in specific intragrain regions (see top panel in Figure 3d). These bromide clusters exhibit higher YM than the parent bulk regions defining mechanical boundaries that enclose mechanical domains in general smaller in size to morphological grains.<sup>[52]</sup> When light is introduced, it provides the required energy to promote ion migration, which happens preferentially at regions

with a high fraction of bromide (see bottom panel in Figure 3d). The mechanical properties of the film are homogenized due to the selective migration of previously clustered bromide ions to become better intermixed with the bulk mixed-halide regions. We acknowledge that the mechanical variations may be influenced by strain gradients between and within grains. However, atomic-scale electron microscopy has recently shown that strain occurring at the (morphological) grain boundaries extends for only a few unit cells.<sup>[53]</sup> We cannot discard that this may have an impact in our observations, but even with the high spatial resolution we achieve ( $\approx 10$  nm) using AFM, we are not able to resolve heterogeneities at the atomic scale. We note that the diffusion coefficient (diffusion lengths) of the A-site cations is at least three orders of magnitude (30 times) smaller than the one of halides, making their movement unlikely to be the origin of the transient phenomena we observe.<sup>[54]</sup> However, the volatile character of the organic molecules, especially MA, the migration of halides down into the film, and the formation of other products such as PbO may play a role in the overall decrease in the average YM upon light soaking (see Figure 2e). Concomitantly, oxygen and light-induced passivation processes involving ion migration reduce the deep trap density and non-radiative recombination processes in the films. This collective effect leads to improved optoelectronic properties expressed as an overall enhancement of the PL lifetimes measured in the films.<sup>[25,26,55]</sup>

### 3. Conclusion

In conclusion, our study reveals that the mechanical properties of triple cation mixed-halide films vary on the submicron scale. These heterogeneities in the YM arise from the presence of stiffer, bromide-rich areas, forming mechanical boundaries that define mechanical domains of a smaller size than morphological grains. These local mechanical properties evolve upon light soaking, with the stiffer mechanical boundaries homogenizing toward the YM values of the bulk of the halide-intermixed perovskite areas. Photobrightening also occurs on a similar timescale as the film stiffness homogenization, suggesting that the mechanical and photophysical properties in mixed-halide perovskites have a common shared origin in compositional heterogeneities. Mechanical properties will become increasingly important as the community focuses on the topics of strain and potential mechanical delamination of layers, especially in complicated device stacks and even modules. The intrinsic processes observed in this work in the absorber layers will thus be limiting mechanisms for operation of full device structures. This study adds to the current understanding of the physical processes governing the working principles of these materials at the nanoscale, demonstrating that their mechanical properties are variable and evolve under relevant in operando conditions.

### 4. Experimental Section

*Fabrication of Perovskite Thin Films:* Triple cation perovskite  $\text{Cs}_{0.05}\text{MA}_{0.17}\text{FA}_{0.78}\text{Pb}(\text{I}_{0.83}\text{Br}_{0.17})_3$  samples were deposited on 200  $\mu\text{m}$  thick

coverslips. Precursor solutions were prepared by dissolving  $\text{PbI}_2$  (1.1 M), formamidinium iodide (FAI, 1 M), methylammonium bromide (MABr, 0.2 M), and  $\text{PbBr}_2$  (0.22 M) in anhydrous DMF:DMSO (4:1 volume ratio). CsI (1.5 M in DMSO) was then added to the precursor solution. A two-step thin-film deposition program was followed at 1000 and 6000 rpm for 10 and 30 s, respectively, and added 100  $\mu\text{L}$  of chlorobenzene 30 s after the start of the spinning routine. The films were annealed at 100  $^\circ\text{C}$  for 1 h. Perovskite synthesis and thin-film deposition were carried out in a  $\text{N}_2$ -filled glovebox to prevent them from degradation. Samples were always transported in hermetically sealed chambers to prevent them from degradation before performing any morphological, structural, mechanical, or photophysical characterization.

*Scanning Electron Microscopy:* An analytical field-emission scanning electron microscope (FEI Nova NanoSEM) was employed to image the morphology of the perovskite films. The authors used an in-lens detector in secondary electron detection mode and the electron beam energy was set at 5 kV.

*X-Ray Diffraction:* X-ray diffraction patterns of the films were obtained with a Bruker D8 advance equipment with a Copper focus X-ray tube ( $K\alpha$ : 1.54  $\text{\AA}$ ). The scan range for  $2\theta$  was from  $10^\circ$  to  $40^\circ$  with a step size of  $0.10^\circ$ .

*Photoluminescence Spectra:* Photoluminescence spectra of the films were acquired using a widefield microscope (IMA VISTM, Photon Etc.). A CW 405 nm laser was employed to excite the samples and emitted light was detected in reflectance mode with a  $20\times$  objective. A tunable Bragg filter was employed to obtain the spectrally resolved maps from 650 to 850 nm with a step size of 2 nm.

*Atomic Force Microscopy:* Topography and YM maps were acquired using a Bruker Bioscope Resolve in PeakForce QNM mode and RTESPA 525 probes (Bruker AFM probes) with a nominal spring constant of 200  $\text{N m}^{-1}$  and resonant frequency of 525 kHz. The spring constant and deflection sensitivity of the probes were calibrated using a sapphire standard sample prior to each measuring session and the tip radius was estimated to be 20–30 nm, using a Titanium sample of known roughness. Topography maps of  $5 \times 5 \mu\text{m}^2$  areas were first acquired and  $2 \times 2 \mu\text{m}^2$  areas within these larger scans were probed with nanomechanical mapping.  $2 \times 2 \mu\text{m}^2$  areas were scanned with 256 lines each, and 256 force curves were acquired within each line (see Figure S5, Supporting Information, for a representative force curve). The extension part of the force curves was fitted to a linearized Hertz model for each pixel using Nanoscope 9.1 (Bruker), and the YM was calculated as described in Extraction of Young's Modulus/Curve Fitting, Supporting Information. We defined mechanical boundaries as clusters of five or more force curves with YM above the global average.

*Time-Resolved Photoluminescence and Correlative Atomic Force Microscopy-Photoluminescence Imaging:* Time-resolved photoluminescence spectroscopy measurements were performed on a home-built, confocal microscope setup equipped with a pulsed supercontinuum source with 2 MHz repetition rate (Fianium Whitelase SC-400-4, 6 ps pulse widths), a  $100\times$  objective lens (LMPlanFL N,  $100\times$  air, 0.8 NA, Olympus, Germany), and a time-correlated single photon counting module (SPC-830, Becker & Hickl GmbH, Germany). A bandpass filter FF01-474/27 was used to select a narrow excitation band and a longpass filter BLP01-635LP (both from Semrock Inc., New York, USA) was used to filter PL emission from the sample. Photons were acquired for 15 min to collect enough photons per pixel in each  $256 \times 256$  time-resolved PL image. The excitation power was maintained below  $2.5 \mu\text{J cm}^{-2} \text{ pulse}^{-1}$ . According to previous references,<sup>[10,56]</sup> this fluence was high enough to saturate the traps and locally create Auger non-radiative effects. Nevertheless, the confocal nature of the measurement may have meant that carriers quickly diffuse and therefore the concentration quickly dilutes down to trap limited regime (which likely reflects the lifetimes one measure).

The time taken for the PL to decay to  $1/e$ <sup>[10,56,57]</sup> of its maximum intensity was calculated as the apparent PL lifetime in each image pixel using a custom MATLAB script. This calculation avoids biases that stem from fitting time-resolved data to mono- and bi-exponential decays. A model-free phasor plot analysis was also performed using SPCImage



v7.4 (Becker & Hickl GmbH, Germany). In this analysis, the PL decay in each image pixel undergoes a Fourier transform at the laser angular frequency to yield a complex variable called the “phasor”.<sup>[49,50]</sup> The phasor coordinates representing the imaginary part and the real part were denoted by  $s$  and  $g$ , respectively, where

$$g_{i,j}(\omega) = \int_0^\infty I_{i,j}(t) \cos(\omega t) dt / \int_0^\infty I_{i,j}(t) dt \quad (1)$$

$$s_{i,j}(\omega) = \int_0^\infty I_{i,j}(t) \sin(\omega t) dt / \int_0^\infty I_{i,j}(t) dt \quad (2)$$

$g_{i,j}(\omega)$  and  $s_{i,j}(\omega)$  were the  $x$  and  $y$  coordinates of the phasor plot as shown in Figure 2h.  $I(t)$  was the time-resolved PL decay,  $\omega$  was  $2\pi$  times the repetition rate of the laser. Thus, the decay from each image pixel  $ij$  could be translated to a point in the 2D phasor plot. Mono-exponential decays lied on the universal circle (blue line, Figure 2h) while complex PL decays as seen in the authors' samples (which depend on trapping, bimolecular recombination and diffusion<sup>[58]</sup>) lied within the universal circle. Any changes to the PL lifetime in a group of pixels led to a displacement of points across the phasor plot. For full detail of plotting lifetime data using the phasor approach, please refer to Digman et al.<sup>[50]</sup>

For correlative AFM-PL imaging, AFM scans were performed first. PL images were captured after flipping the sample upside down for imaging in the inverted microscope frame and scanning the excitation laser over the same perovskite surface (see Figure S4, Supporting Information). The regions of interest from both measurements were registered using signals from markers (gold nanoparticles or scratches) that were easily distinguishable in both the AFM and PL images.

**Nano X-Ray Fluorescence:** nXRF experiments were performed at the Hard X-ray Nanoprobe at the I14 beamline at Diamond Light Source Ltd., Didcot, UK as described previously.<sup>[59,60]</sup> Briefly, horizontal mirrors shaped an X-ray beam from an undulator source onto a secondary source. The beam then passed over a Si monochromator which selected the chosen beam energy of 20 keV. Finally, the beam was incident upon a pair of Kirkpatrick–Baez mirrors which focused the beam down to a size of  $\approx 50 \times 50 \text{ nm}^2$ . Perovskite samples for nXRF characterization were deposited as described above in a PTAA covered<sup>[61]</sup> 200  $\mu\text{m}$  thick,  $7.5 \times 7.5 \text{ mm}^2$  SiN grids with a  $1 \times 1 \text{ mm}^2$ , 100 nm thick window. The sample was placed at the focal point of the beam and was raster scanned across this point. X-ray fluorescence was then captured by a silicon drift detector (Rayspec).

The multidimensional nXRF data were analyzed using DAWN,<sup>[62]</sup> and a combination of Python packages, including Hyperspy.<sup>[63]</sup> The intensity of the Br  $K\alpha$  line and the Pb  $L\alpha$  lines were normalized to their respective means across the entire scan region. Then the normalized Br signal was divided by Pb to get the relative ratio of Br:Pb. It was noted that nXRF measurements did not induce any of the observed Br heterogeneities across the sample.<sup>[52]</sup> It was also noted that the nXRF measurements were not performed in the same samples employed for QNM-AFM. However, all samples were fabricated in the same batch, ensuring reproducible stoichiometry and morphologies.

**Light Soaking:** Light soaking was performed either for 2 or 12 h using a white-light LED source (Xlamp XP-E2 LEDs, Cree Inc.). The source provided 0.375 W power distributed in an area of  $1 \text{ cm} \times 1 \text{ cm}^2$ , leading to a total fluence of  $375 \text{ mW cm}^{-2}$ . This was an illumination equivalent to  $\approx 3.75$  suns (assuming solar illumination was  $100 \text{ mW cm}^{-2}$ ). To quantify the YM across the whole film before light exposure and after 2 and 12 h of light exposure, 10 000 force curves were fitted for each condition. The LED used for light soaking was turned off during PL acquisition. It was noted that one cannot exclude local heating of the absorber layer under these measurements but such a situation represented device-relevant conditions. Nevertheless, only small fluctuations in the sample holder temperature (between 24.7 and 25.8 °C over 3 h of illumination) were observed, thus allowing the authors to exclude extreme thermal fluctuations during the measurements.

## Supporting Information

Supporting Information is available from the Wiley Online Library or from the author.

## Acknowledgements

I.M. and C.P. contributed equally to this work. This project had received funding from the European Union's H2020-MSCA-ITN-2016 research and innovation programme under the Marie Skłodowska-Curie Grant Agreement No. 722380 (SUPUVIR). This project had received funding from the European Research Council (ERC) under the European Union's Horizon 2020 research and innovation programme (grant agreement number 756962). M.A. acknowledges funding from the European Union's Horizon 2020 research and innovation programme under the Marie Skłodowska-Curie grant agreement No. 841386. C.F.K. acknowledges funding from the Engineering and Physical Sciences Research Council, EPSRC (EP/H018301/1 and EP/L015889/1); Wellcome Trust (089703/Z/09/Z and 3–3249/Z/16/Z); Medical Research Council, MRC (MR/K015850/1 and MR/K02292X/1); MedImmune; and Infinitus (China), Ltd. S.D.S. acknowledges support from the Royal Society and Tata Group (UF150033). G.D. acknowledges the Royal Society for funding through a Newton International Fellowship and the EPSRC (EP/R023980/1). K.F. acknowledges George and Lilian Schiff Studentship, Winton Studentship, the Engineering and Physical Sciences Research Council (EPSRC) studentship, Cambridge Trust Scholarship, and Robert Gardiner Scholarship. S.M. acknowledges an EPSRC studentship. T.A.S.D. acknowledges a National University of Ireland Travelling Studentship. A.S. acknowledges NanoDTC ESPSRC Grant (EP/S022953/1). The authors acknowledge the Diamond Light Source (Didcot, UK) for providing beamtime at the Hard X-ray Nanoprobe at I14 beamline (proposal: sp20420) and Julia Parker and Paul Quinn for beamline assistance.

## Conflict of Interest

SDS is a cofounder of Swift Solar Inc.

## Data Availability Statement

The data that support the findings of this study are available from the corresponding author upon reasonable request.

## Keywords

halide perovskites, multimodal imaging, nanomechanical mapping, nanoscale heterogeneities, polycrystalline thin films

Received: February 25, 2021  
Published online: March 31, 2021

- [1] M. Liu, M. B. Johnston, H. J. Snaith, *Nature* **2013**, 501, 395.
- [2] J. Luo, J.-H. Im, M. T. Mayer, M. Schreier, M. K. Nazeeruddin, N.-G. Park, S. D. Tilley, H. J. Fan, M. Grätzel, *Science* **2014**, 345, 1593.
- [3] M. Yuan, L. N. Quan, R. Comin, G. Walters, R. Sabatini, O. Voznyy, S. Hoogland, Y. Zhao, E. M. Beauregard, P. Kanjanaboos, Z. Lu, D. H. Kim, E. H. Sargent, *Nat. Nanotechnol.* **2016**, 11, 872.

- [4] K. Lin, J. Xing, L. N. Quan, F. P. G. de Arquer, X. Gong, J. Lu, L. Xie, W. Zhao, D. Zhang, C. Yan, *Nature* **2018**, 562, 245.
- [5] NREL Photovoltaics Efficiency Chart, <https://www.nrel.gov/pv/assets/pdfs/best-research-cell-efficiencies.20191106.pdf> (accessed: November 2019).
- [6] K. X. Steirer, P. Schulz, G. Teeter, V. Stevanovic, M. Yang, K. Zhu, J. J. Berry, *ACS Energy Lett.* **2016**, 1, 360.
- [7] S. De Wolf, J. Holovsky, S.-J. Moon, P. Löper, B. Niesen, M. Ledinsky, F.-J. Haug, J.-H. Yum, C. Ballif, *J. Phys. Chem. Lett.* **2014**, 5, 1035.
- [8] H. Diab, C. Arnold, F. Lédée, G. Trippé-Allard, G. Delpont, C. Vilar, F. Bretenaker, J. Barjon, J.-S. Lauret, E. Deleporte, *J. Phys. Chem. Lett.* **2017**, 8, 2977.
- [9] S. D. Stranks, G. E. Eperon, G. Grancini, C. Menelaou, M. J. P. Alcocer, T. Leijtens, L. M. Herz, A. Petrozza, H. J. Snaith, *Science* **2013**, 342, 341.
- [10] C. Stavrakas, G. Delpont, A. A. Zhumekenov, M. Anaya, R. Chahbazian, O. M. Bakr, E. S. Barnard, S. D. Stranks, *ACS Energy Lett.* **2020**, 5, 117.
- [11] G. Delpont, S. Macpherson, S. D. Stranks, *Adv. Energy Mater.* **2020**, 1903814.
- [12] M. Xiao, F. Huang, W. Huang, Y. Dkhissi, Y. Zhu, J. Etheridge, A. Gray-Weale, U. Bach, Y. Cheng, L. Spiccia, *Angew. Chem., Int. Ed.* **2014**, 53, 9898.
- [13] J. Even, L. Pedesseau, J.-M. Jancu, C. Katan, *J. Phys. Chem. Lett.* **2013**, 4, 2999.
- [14] B. Saparov, D. B. Mitzi, *Chem. Rev.* **2016**, 116, 4558.
- [15] E. M. Tennyson, T. A. S. Doherty, S. D. Stranks, *Nat. Rev. Mater.* **2019**, 4, 573.
- [16] T. A. S. Doherty, A. J. Winchester, S. Macpherson, D. N. Johnstone, V. Pareek, E. M. Tennyson, S. Kosar, F. U. Kosasih, M. Anaya, M. Abdi-Jalebi, Z. Andaji-Garmaroudi, E. L. Wong, J. Madéo, Y.-H. Chiang, J.-S. Park, Y.-K. Jung, C. E. Petoukhoff, G. Divitini, M. K. L. Man, C. Ducati, A. Walsh, P. A. Midgley, K. M. Dani, S. D. Stranks, *Nature* **2020**, 580, 360.
- [17] E. Ruggeri, M. Anaya, K. Gałkowski, G. Delpont, F. U. Kosasih, A. Abfalterer, S. Mackowski, C. Ducati, S. D. Stranks, *Adv. Mater.* **2019**, 31, 1905247.
- [18] M. Saliba, T. Matsui, J. Y. Seo, K. Domanski, J. P. Correa-Baena, M. K. Nazeeruddin, S. M. Zakeeruddin, W. Tress, A. Abate, A. Hagfeldt, M. Grätzel, *Energy Environ. Sci.* **2016**, 9, 1989.
- [19] Y. Hou, E. Aydin, M. De Bastiani, C. Xiao, F. H. Isikgor, D.-J. Xue, B. Chen, H. Chen, B. Bahrami, A. H. Chowdhury, A. Johnston, S.-W. Baek, Z. Huang, M. Wei, Y. Dong, J. Troughton, R. Jalmood, A. J. Mirabelli, T. G. Allen, E. Van Kerschaver, M. I. Saidaminov, D. Baran, Q. Qiao, K. Zhu, S. De Wolf, E. H. Sargent, *Science* **2020**, 367, 1135.
- [20] W. Li, M. U. Rothmann, A. Liu, Z. Wang, Y. Zhang, A. R. Pascoe, J. Lu, L. Jiang, Y. Chen, F. Huang, Y. Peng, Q. Bao, J. Etheridge, U. Bach, Y.-B. Cheng, *Adv. Energy Mater.* **2017**, 7, 1700946.
- [21] T. W. Jones, A. Osherov, M. Alsari, M. Sponseller, B. C. Duck, Y.-K. Jung, C. Settens, F. Niroui, R. Brenes, C. V. Stan, *Energy Environ. Sci.* **2019**, 12, 596.
- [22] J.-P. Correa-Baena, Y. Luo, T. M. Brenner, J. Snaider, S. Sun, X. Li, M. A. Jensen, N. T. P. Hartono, L. Nienhaus, S. Wiegold, J. R. Poindexter, S. Wang, Y. S. Meng, T. Wang, B. Lai, M. V. Holt, Z. Cai, M. G. Bawendi, L. Huang, T. Buonassisi, D. P. Fenning, *Science* **2019**, 363, 627.
- [23] S. Feldmann, S. Macpherson, S. P. Senanayak, M. Abdi-Jalebi, J. P. H. Rivett, G. Nan, G. D. Tainter, T. A. S. Doherty, K. Frohna, E. R. Sange, R. H. Friend, H. Sirringhaus, M. Saliba, D. Beljonne, S. D. Stranks, F. Deschler, *Nat. Photonics* **2019**, 14, 123.
- [24] E. T. Hoke, D. J. Slotcavage, E. R. Dohner, A. R. Bowring, H. I. Karunadasa, M. D. McGehee, *Chem. Sci.* **2015**, 6, 613.
- [25] Z. Andaji-Garmaroudi, M. Abdi-Jalebi, D. Guo, S. Macpherson, A. Sadhanala, E. M. Tennyson, E. Ruggeri, M. Anaya, K. Galkowski, R. Shivanna, K. Lohmann, K. Frohna, S. Mackowski, T. J. Savenije, R. H. Friend, S. D. Stranks, *Adv. Mater.* **2019**, 31, 1902374.
- [26] Z. Andaji-Garmaroudi, M. Anaya, A. J. Pearson, S. D. Stranks, *Adv. Energy Mater.* **2020**, 10, 1903109.
- [27] W. Hui, Y. Xu, F. Xia, H. Lu, B. Li, L. Chao, T. Niu, B. Du, H. Du, X. Ran, *Nano Energy* **2020**, 73, 104803.
- [28] D.-J. Xue, Y. Hou, S.-C. Liu, M. Wei, B. Chen, Z. Huang, Z. Li, B. Sun, A. H. Proppe, Y. Dong, M. I. Saidaminov, S. O. Kelley, J.-S. Hu, E. H. Sargent, *Nat. Commun.* **2020**, 11, 1514.
- [29] H. Jin, J. Li, Y. Dai, Y. Wei, *Phys. Chem. Chem. Phys.* **2017**, 19, 4855.
- [30] Q. Tu, I. Spanopoulos, E. S. Vasileiadou, X. Li, M. G. Kanatzidis, G. S. Shekawat, V. P. Dravid, *ACS Appl. Mater. Interfaces* **2020**, 12, 20440.
- [31] A. C. Ferreira, A. Létoublon, S. Paofai, S. Raymond, C. Ecolivet, B. Rufflé, S. Cordier, C. Katan, M. I. Saidaminov, A. A. Zhumekenov, *Phys. Rev. Lett.* **2018**, 121, 85502.
- [32] T.-H. Fang, W.-J. Chang, C.-M. Lin, *Microelectron. Eng.* **2005**, 77, 389.
- [33] Y. Rakita, S. R. Cohen, N. K. Kedem, G. Hodes, D. Cahen, *MRS Commun.* **2015**, 5, 623.
- [34] S. Sun, Y. Fang, G. Kieslich, T. J. White, A. K. Cheetham, *J. Mater. Chem. A* **2015**, 3, 18450.
- [35] S. Sun, F. H. Isikgor, Z. Deng, F. Wei, G. Kieslich, P. D. Bristowe, J. Ouyang, A. K. Cheetham, *ChemSusChem* **2017**, 10, 3740.
- [36] A. A. Bukharaev, A. K. Zvezdin, A. P. Pyatakov, Y. K. Fetisov, *Phys.-Usp.* **2018**, 61, 1175.
- [37] W. Wei, Y. Dai, B. Huang, *Phys. Chem. Chem. Phys.* **2017**, 19, 663.
- [38] L. Shu, S. Ke, L. Fei, W. Huang, Z. Wang, J. Gong, X. Jiang, L. Wang, F. Li, S. Lei, *Nat. Mater.* **2020**, 19, 605.
- [39] R. Maranganti, P. Sharma, *Phys. Rev. B* **2009**, 80, 54109.
- [40] Y. Liu, I. Sokolov, M. E. Dokukin, Y. Xiong, P. Peng, *Nanoscale* **2020**, 12, 12432.
- [41] T. Namazu, Y. Isono, T. Tanaka, *J. Microelectromech. Syst.* **2000**, 9, 450.
- [42] D. J. Fairfield, H. Sai, A. Narayanan, J. V. Passarelli, M. Chen, J. Palasz, L. C. Palmer, M. R. Wasielewski, S. I. Stupp, *J. Mater. Chem. A* **2019**, 7, 1687.
- [43] G. Han, H. D. Hadi, A. Bruno, S. A. Kulkarni, T. M. Koh, L. H. Wong, C. Soci, N. Mathews, S. Zhang, S. G. Mhaisalkar, *J. Phys. Chem. C* **2018**, 122, 13884.
- [44] M. Thambidurai, S. Foo, K. M. M. Salim, P. C. Harikesh, A. Bruno, N. F. Jamaludin, S. Lie, N. Mathews, C. Dang, *J. Mater. Chem. C* **2019**, 7, 5028.
- [45] S. Jariwala, H. Sun, G. W. P. Adhyaksa, A. Lof, L. A. Muscarella, B. Ehrler, E. C. Garnett, D. S. Ginger, *Joule* **2019**, 3, 3048.
- [46] V. Kumar, W. L. Schmidt, G. Schileo, R. C. Masters, M. Wong-Stringer, D. C. Sinclair, I. M. Reaney, D. Lidzey, C. Rodenburg, *ACS Omega* **2017**, 2, 2126.
- [47] E. M. Hutter, L. A. Muscarella, F. Wittmann, J. Versluis, L. McGovern, H. J. Bakker, Y.-W. Woo, Y.-K. Jung, A. Walsh, B. Ehrler, *Cell Rep. Phys. Sci.* **2020**, 1, 100120.
- [48] A. Jaffe, Y. Lin, C. M. Beavers, J. Voss, W. L. Mao, H. I. Karunadasa, *ACS Cent. Sci.* **2016**, 2, 201.
- [49] S. Ranjit, L. Malacrida, D. M. Jameson, E. Gratton, *Nat. Protoc.* **2018**, 13, 1979.
- [50] M. A. Digman, V. R. Caiolfa, M. Zamai, E. Gratton, *Biophys. J.* **2008**, 94, L14.
- [51] M. I. Saidaminov, K. Williams, M. Wei, A. Johnston, R. Quintero-Bermudez, M. Vafaie, J. M. Pina, A. H. Proppe, Y. Hou, G. Walters, *Nat. Mater.* **2020**, 19, 412.
- [52] Y. Luo, P. Khoram, S. Brittman, Z. Zhu, B. Lai, S. P. Ong, E. C. Garnett, D. P. Fenning, *Adv. Mater.* **2017**, 29, 1703451.



- [53] M. U. Rothmann, J. S. Kim, J. Borchert, K. B. Lohmann, C. M. O'Leary, A. A. Sheader, L. Clark, H. J. Snaith, M. B. Johnston, P. D. Nellist, L. M. Herz, *Science* **2020**, *370*, eabb5940.
- [54] A. Senocrate, I. Moudrakovski, G. Y. Kim, T.-Y. Yang, G. Gregori, M. Grätzel, J. Maier, *Angew. Chem., Int. Ed.* **2017**, *56*, 7755.
- [55] M. Anaya, J. F. Galisteo-López, M. E. Calvo, J. P. Espinós, H. Míguez, *J. Phys. Chem. Lett.* **2018**, *9*, 3891.
- [56] S. D. Stranks, V. M. Burlakov, T. Leijtens, J. M. Ball, A. Goriely, H. J. Snaith, *Phys. Rev. Appl.* **2014**, *2*, 34007.
- [57] C. Stavrakas, A. A. Zhumekenov, R. Brenes, M. Abdi-Jalebi, V. Bulović, O. M. Bakr, E. S. Barnard, S. D. Stranks, *Energy Environ. Sci.* **2018**, *11*, 2846.
- [58] D. W. de Quilettes, S. M. Vorpahl, S. D. Stranks, H. Nagaoka, G. E. Eperon, M. E. Ziffer, H. J. Snaith, D. S. Ginger, *Science* **2015**, *348*, 683.
- [59] M. A. Gomez-Gonzalez, M. A. Koronfel, A. E. Goode, M. Al-Ejji, N. Voulvoulis, J. E. Parker, P. D. Quinn, T. B. Scott, F. Xie, M. L. Yallop, A. E. Porter, M. P. Ryan, *ACS Nano* **2019**, *13*, 11049.
- [60] P. Quinn, J. Parker, F. Cacho-Nerin, M. Walker, P. Howes, *Microsc. Microanal.* **2018**, *24*, 244.
- [61] Z. Liu, L. Krückemeier, B. Krogmeier, B. Klingebiel, J. A. Márquez, S. Levchenko, S. Öz, S. Mathur, U. Rau, T. Unold, T. Kirchartz, *ACS Energy Lett.* **2019**, *4*, 110.
- [62] M. Basham, J. Filik, M. T. Wharmby, P. C. Y. Chang, B. El Kassaby, M. Gerring, J. Aishima, K. Levik, B. C. A. Pulford, I. Sikharulidze, D. Sneddon, M. Webber, S. S. Dhesi, F. Maccherozzi, O. Svensson, S. Brockhauser, G. Naray, A. W. Ashton, *J. Synchrotron Radiat.* **2015**, *22*, 853.
- [63] HyperSpy v1.5.2, <https://doi.org/10.5281/zenodo.3396791> (accessed: September 2019).